

# ReLayNet: Retinal Layer and Fluid Segmentation of Macular Optical Coherence Tomography using Fully Convolutional Network

Abhijit Guha Roy<sup>\*a,b,d</sup>, Sailesh Conjeti<sup>\*a</sup>, Sri Phani Krishna Karri<sup>b</sup>, Debdoot Sheet<sup>b</sup>, Amin Katouzian<sup>c</sup>, Christian Wachinger<sup>d</sup>, Nassir Navab<sup>a,e</sup>

<sup>a</sup>Computer Aided Medical Procedures, Technische Universität München, Munich, Germany

<sup>b</sup>Indian Institute of Technology Kharagpur, WB, India

<sup>c</sup>IBM Almaden Research Center, Almaden, USA.

<sup>d</sup>Department of Child and Adolescent Psychiatry, Psychosomatic and Psychotherapy, Ludwig Maximilian University, Munich, Germany

<sup>e</sup>Computer Aided Medical Procedures, Johns Hopkins University, USA.

**Abstract.** Optical coherence tomography (OCT) is extensively used for diagnosis of diabetic macular edema due to its non-invasive imaging based assessment of the retinal layers. In this paper, we propose a new fully convolutional deep learning architecture, termed ReLayNet, for segmentation of retinal layers and fluid masses in eye OCT scans. ReLayNet uses a contracting path of convolutional blocks (encoders) to learn a hierarchy of contextual features, followed by an expansive path of convolutional blocks (decoders) for semantic segmentation. Additionally, skip connections relaying encoder outputs to matched decoder inputs are introduced to recover spatial information lost during downsampling. ReLayNet is trained with stochastic gradient descent to optimize a joint loss function comprising of both weighted logistic regression and Dice overlap loss. The framework is validated on a publicly available benchmark dataset with comparisons against five state-of-the-art segmentation methods which includes two deep learning based approaches. Additionally, eight incremental baselines are defined and compared with, to validate the individual contributions of the proposed framework. We demonstrate that ReLayNet can reliably segment the retinal layers and accumulated fluids with improved performance in retinal thickness estimation and contour delineation. With a segmentation time of 5s per volume, it is well suited for clinical applications.

**Keywords:** Optical coherence tomography, retinal layer segmentation, deep learning, diabetic macular edema.

\*Equal Contribution

## 1 Introduction

Spectral Domain Optical Coherence Tomography (SD-OCT) is a non-invasive imaging modality commonly used for acquiring high resolution ( $6\mu\text{m}$ ) cross-sectional scans for biological tissues with sufficient depth of penetration ( $0.5 - 2\text{ mm}$ ).<sup>1,2</sup> It uses the principle of speckle formation through coherence sensing of photons backscattered within highly scattering optical media like biological soft tissues<sup>3</sup> for the purpose of image formation. It has found its application in medical imaging ranging across retinal pathology investigation, to skin imaging for monitoring wound healing<sup>4</sup> and intravascular imaging for effective stent placement,<sup>5</sup> lumen detection<sup>6</sup> and plaque detection.<sup>7,8</sup> OCT is the preferred modality of choice for cross-sectional imaging of the retina on account of its high resolution favoring clear visualization of the various constituent layers of the retina. This allows their mapping and thickness measurements. These help in diagnosing retinal ailments and plan treatment guidance for glaucoma and retinal diseases, such as age-related macular degeneration (AMD) and diabetic retinopathy (DR).

Diabetes is a widely occurring chronic, metabolic disease with an estimated incidence in about 415 million people (roughly 8.3% of human adult population).<sup>9</sup> Diabetic individuals often are under high risk of developing vision-related co-morbidities, which is reported at a significant 28%.<sup>10</sup>

The degradation of quality of vision in diabetics is often associated to DR, which results in damage of retinal blood vessels. Hyperglycemia (abnormally high blood glucose levels) in diabetic patients leads to the rupture of the vascular epithelial and mural cells between the blood vessels and retina.<sup>11</sup> Further, the retinal fluid transport cells are also damaged over time. Due to this, the leaked out fluid tends to accumulate between the retinal layers.<sup>12</sup> When left untreated, severe hypertension within retinal blood vessels and fluid build-up resulting in manifestations of diabetic macular edema (DME)<sup>13</sup> which leads to vision impairment. Thus, proper monitoring of the retinal layer morphology and fluid accumulation is necessary for diabetic patients to prevent chances of occurrence of blindness.

Acquisition of retinal OCT centered at the optical nerve and fovea is highly challenging due to the presence of micro-saccadic eye movements resulting in motion artifacts, variations in tissue inclination with respect to the coherence wave surface and poor signal to noise ratio with increasing imaging depth. The acquisition is also particularly difficult in cases of highly myopic eyes. These inherent challenges associated with the modality makes the interpretation of an OCT image difficult and often highly variable among experts. Specifically, due to the highly diffused nature of the boundaries between two retinal layers. This causes manual annotation of the layer boundaries to be very subjective and time consuming. This has motivated a lot of research for developing automated methods for segmenting different retinal layers from OCT images and aid in accurate diagnosis with minimum subject variation in reporting.<sup>14–18</sup>

Towards this end, we propose a deep learning based end-to-end learning framework for segmentation of multiple retinal layers and delineation of fluid pockets in eye OCT images, called ReLayNet (short for *Retinal Layer* segmentation network). To the best of our knowledge, this is the first time deep learning based fully convolutional end-to-end method is leveraged towards this application. Fig. 1 previews the results of the proposed ReLayNet for two OCT slices (Fig. 1(c) and (f)) showing distinctive layers of the retina with their annotations (Fig. 1(b) and (e)), with one normal slice (Fig. 1(a)) and another showing edematous manifestations due to DR (Fig. 1(d)).

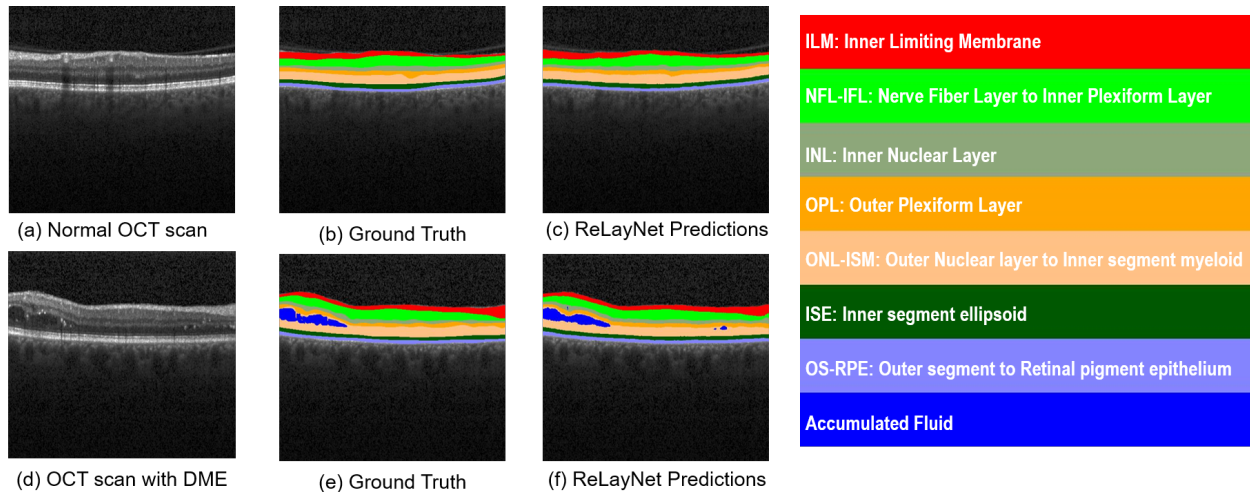


**Fig 1** Segmentation results of the proposed ReLayNet of OCT frames without and with edema. OCT frame with no edema, its ground truth and ReLayNet segmentation are shown in (a), (b) and (c) respectively. OCT frame with edema, its ground truth and RelayNet predictions are shown in (d), (e) and (f) respectively. The tissue types corresponding to each colors are presented to the right.

## 2 State of the art

The segmentation of a retinal OCT scan involves assigning each image pixel a label. Traditionally, patch-based approaches have been used that predict the center label for each patch separately. Testing in such a scenario involves a sliding window based scanning of the slice and labelling the pixels accordingly. The main issues with such patch based approaches are: (i) predictions are based on information of the local patch and not on context represented by the whole image, (ii) testing phase could be slow which limits its potential for deployment in time-constrained settings (like during interventions). With the main focus of addressing these issues, in this work we aim at generating layer segmentations of a whole B-scan slice in an end-to-end fashion, in effect leveraging the complete context presented by a particular image scan. Deep learning based approaches provide the advantage of learning discriminative representations from the data sans the need for handcrafting features. In particular, we propose a deep learning architecture that falls under the family of fully convolutional neural networks (F-CNN) that are specifically tailored for semantic segmentation which predicts the label for all the image pixel together.<sup>19-21</sup> As the main focus of this work involves developing a deep learning based method for semantic segmentation of retinal OCT images, we present the prior art for each of these areas in the following sections.

### 2.1 Retinal Layer Segmentation

Most of the existing methods for OCT can be broadly categorized into (a) Graph based methods and (b) Non graph based approaches which includes A-scan analysis, active contours, probabilistic models etc. **Graph based approaches:** Most of the existing methods for OCT retinal layer segmentation are based on graph based approaches coupled with dynamic programming.<sup>14-18</sup> Chiu *et al.* proposed one of the earliest methods towards this task that leverages intensity gradients to estimate the edge weights of a graph based representation of the OCT image, followed by dynamic programming to find the shortest path from one node to another, thus estimating the layer boundaries.<sup>15</sup> It was further improved in a subsequent method by using hard and soft constraints to add prior information from a learned model while constructing the graph edges followed by dynamic programming for segmentation.<sup>18</sup> Alternately, Srinivasan *et al.* proposed using sparsity based image denoising, support vector machines, heuristic prior for the graph construction and dynamic programming based segmentation in two stages to ease the task at hand.<sup>16</sup> A relatively recent work Chiu *et al.* demonstrates the use of kernel regression based methods to classify the layers and fluid masses and then in a second stage refining the estimates with graph based dynamic programming method.<sup>17</sup> Following on similar lines, Karri *et al.* proposed to reinforce graph based segmentation by learning layer specific edges using structured random forests.<sup>22</sup> Also, recent work by Chiu *et al.* modified the dynamic programming based approach in,<sup>15</sup> by considering the spatial dependency of the frame to its two adjacent frame.<sup>23</sup>

**Non-graph approaches:** Some of the existing methods uses peak and valley points in each A-scans of a OCT frame followed by model fitting to achieve retinal layer segmentation.<sup>24-26</sup> Some non-dynamic programming based techniques proposed for retinal layer segmentation that involve the use of texture information together with diffusion maps<sup>14</sup> and probabilistic approach for modelling retinal layers using layer boundary specific shape regularizers.<sup>27</sup> It also includes using two parallel active contours acting simultaneously to segment the retinal boundaries.<sup>28</sup>

**Limitations:** The above frameworks proposed towards retinal layer segmentation are not end-to-end paradigms. Often, heuristics and hand-crafting is employed in choosing the graph weights for

dynamic programming. The segmentation is achieved in multiple stages involving pre-processing stages like denoising and post-processing stages of refinement. Though these additional steps do not limit the usability of these methods, it must be noted that these require significant domain knowledge and modelling approximations. Also, methods often did not consider the presence of fluid filled regions while learning to do layer segmentation. This could lead to potentially erroneous layer segmentations in presence of pathology like DME. To address the aforementioned limitations, we employ deep learning to learn a data-driven end-to-end model for simultaneous segmentation of retinal layers and fluid masses within an OCT image.

## 2.2 Deep Learning for Semantic Segmentation

Recently, there have been a considerable amount of work for semantic segmentation using deep learning methods within the computer vision and medical imaging communities. The seminal work on fully convolutional semantic segmentation proposed by Long *et al.*<sup>19</sup> is particularly relevant in the context of this work. They leveraged a deep network pre-trained for the task of classification, combined with different resolution feature maps by interpolating them all to the size of the image and learn to perform segmentation.<sup>19</sup> A significant improvement over this model was achieved by using an encoder-decoder based framework for semantic segmentation, termed as DeconvNet and the introduction of unpooling layers instead of interpolation to improve the spatial consistency of segmentation.<sup>20</sup> In an alternate work, Chen *et al.* proposed the concept of using atrous convolutional kernels instead of interpolation to get much smoother version of feature maps that are better suited for semantic segmentation.<sup>29</sup> Within the medical imaging community, Ronnerberger *et al.* proposed the U-Net architecture that leverages an encoder-decoder architecture and introduces skip connections across them.<sup>21</sup> They demonstrate that such an architecture can be trained in presence of limited training data when appropriate data augmentation schemes are employed. It must be noted that the architecture presented in this work is inspired in part by U-Net<sup>21</sup> and DeconvNet.<sup>20</sup>

## 2.3 Contributions

The salient contributions presented in the paper can be listed as:

1. To the best of our knowledge, this is the first work employing fully-convolutional deep learning approach for fine-grained layer and fluid segmentation in retinal OCT images.
2. ReLayNet is an end-to-end learning approach that is driven entirely by the OCT data without employing any heuristics or hand-crafting of features. It is fully-convolutional in nature and is relatively faster as it does not employ expensive optimization routines during testing.
3. Our model uses an encoder-decoder configuration which is tailored for the task at hand by incorporation of unpooling stages with skip connections for improved spatial consistency and ease of gradient flow during training.
4. ReLayNet is trained with a composite loss function comprising of a weighted logistic regression loss along with Dice loss for improved segmentation. The weighting scheme employed effectively compensates for the problem of class imbalance and selectively penalizes misclassification at layer boundaries. This in turn encourages learning of a hierarchy of features that are tuned to discriminate layer transitions effectively.

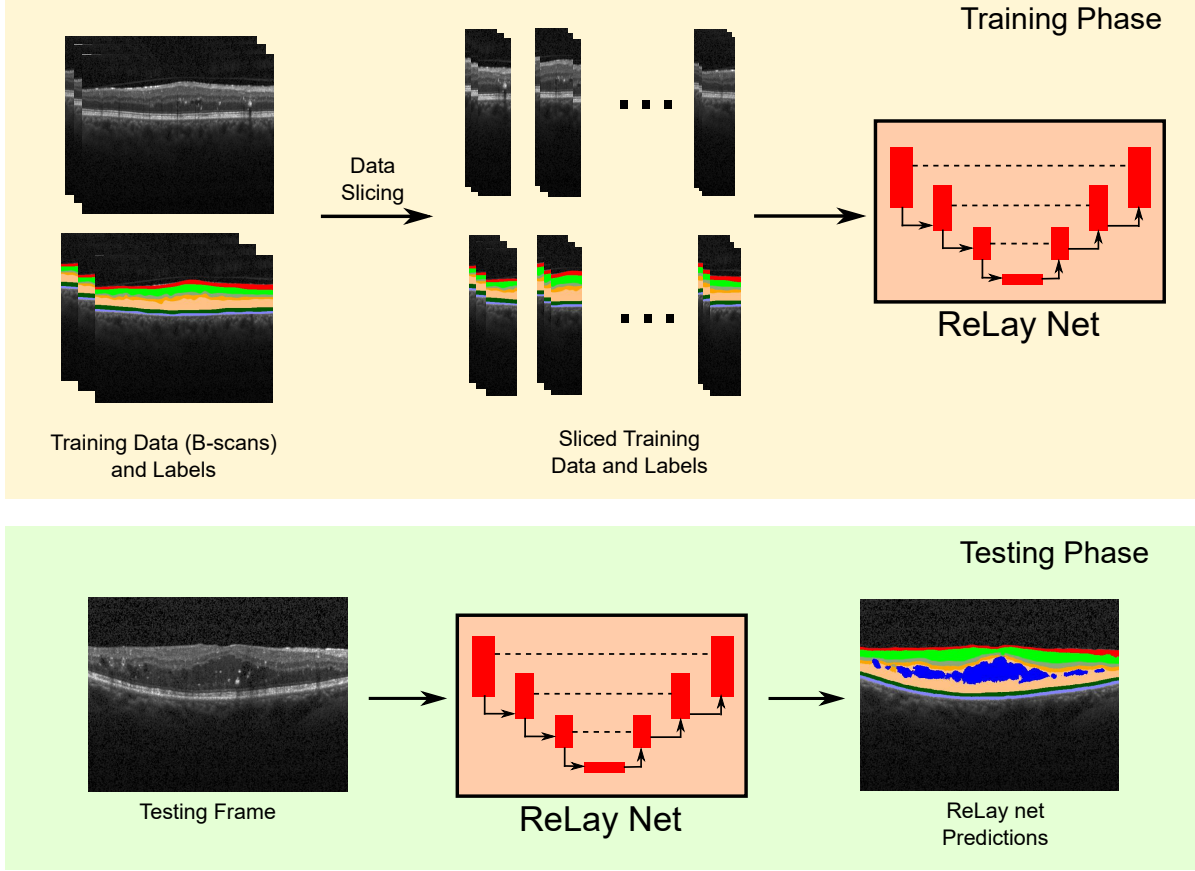


**Fig 2** Overall flow of the training and testing procedure for the proposed ReLayNet. The training procedure involves slicing of the OCT B-scans as shown above. The testing phase doesn't involve this stage due to the fully-convolutional nature of the proposed ReLayNet.

We detail the methodology of the proposed framework in Sec. 3. The experimental setup is introduced in Sec. 4. The results are reported and discussed in Sec. 5 and finally the conclusion is presented in Sec. 6.

### 3 Methodology

#### 3.1 Problem Statement

Given a retinal OCT image  $\mathcal{I}$ , the task is to assign each pixel location  $\mathbf{x} = (r, c)$  to a particular label  $l$  in the label space  $\mathcal{L} = \{l\} = \{1, \dots, K\}$  for  $K$  classes. We treat the segmentation task as a  $K = 10$  class classification problem. The tissue classes are: [Cls 1:] Region above the retina (RaR); [Cls 2:] ILM: Inner limiting membrane; [Cls 3:] NFL-IPL: Nerve fiber ending to Inner plexiform layer; [Cls 4:] INL: Inner Nuclear layer; [Cls 5:] OPL: Outer plexiform layer; [Cls 6:] ONL-ISM: Outer Nuclear layer to Inner segment myeloid; [Cls 7:] ISE: Inner segment ellipsoid; [Cls 8:] OS-RPE: Outer segment to Retinal pigment epithelium; [Cls 9:] Region below RPE (RbR) and [Cls 10:] Fluid region (shown in Fig. 1).



### 3.2 OCT B-scan slicing and data augmentation

Training of a deep ReLayNet model on large images is limited by the available RAM in the GPU. One possible way to avoid this issue is to train with smaller batch size, but it often leads to very noisy gradients while training and the loss curve tend to diverge.<sup>30</sup> To address this issue, we used a data slicing approach. Given an OCT B-scan  $\mathcal{I}$  of size  $M \times N$ , we divide each B-scan into  $G$ ,  $M \times G'$  slices by taking several non-overlapping  $G'$  A-scan lines at a time. Further, we augment the sliced data by introducing random horizontal flips and slight spatial translations and cropping. This creates invariance to these transformations within the network. It must be noted that due to the fully convolutional nature of the ReLayNet architecture, the size of input and segmented output has the same dimensions. This also allows for using the whole B-scan image during testing to obtain a seamless segmentation without any slicing induced artifacts.

### 3.3 Network Architecture

The network architecture of the proposed ReLayNet is illustrated in Figure 3. This architecture is in part inspired by two popular prior deep learning architectures, namely, DeConvnet<sup>20</sup> and U-Net.<sup>21</sup> It consists of a contracting path of encoder blocks followed by an expansive path of decoder blocks with skip connections relaying the intermittent feature representations from encoder blocks to their matched decoder blocks through concatenation layers. In particular, we leverage the skip connections introduced in U-Net<sup>21</sup> and unpooling layers proposed in Deconvnet<sup>20</sup> for upsampling the output of the decoder blocks. In this work, the proposed architecture consists of three encoder blocks with their matched decoder blocks followed by a classification layer. The individual constituent blocks are explained in detail below.

#### 3.3.1 Encoder block

Each encoder block consist of 4 main layers: (i) convolution layer, (ii) batch normalization layer, (iii) ReLU activation layer and (iv) max pooling layer. The convolution kernels for all the encoder blocks are defined of rectangular size  $7 \times 3$  due to rectangular sliced training data, along with bias. The kernel size is choosen to make sure the receptive field at the last encoder block encompasses the whole retinal region. The feature maps are appropriately zero padded so that the dimension before and after the convolution layer remains the same. A batch normalization layer is introduced after the convolution layer to compensate for the covariate shifts and prevent overfitting during the training procedure.<sup>30</sup> ReLU introduces non-linearity in the training. This is followed by a max pooling layer which reduces the height and width of the feature map by half. The pooling indices during max pooling are stored which are in-turn used in the unpooling stage of decoder block to preserve spatial consistency.

#### 3.3.2 Decoder Block

Each decoder block consists of 5 main layers: (i) unpooling layer, (ii) concatenation layer (iii) convolution layer, (iv) batch normalization and (v) ReLU activation function. The Unpooling layer upsamples a lower resolution feature map to a higher resolution one. It utilizes the the saved pooling indices in the matched encoder block for upsampling the output of the previous decoder block from lower resolution to a higher one by mapping it to appropriate spatial positions. The rest is filled with zeros. This process is illustrated schematically in Fig. 4. Such an unpooling

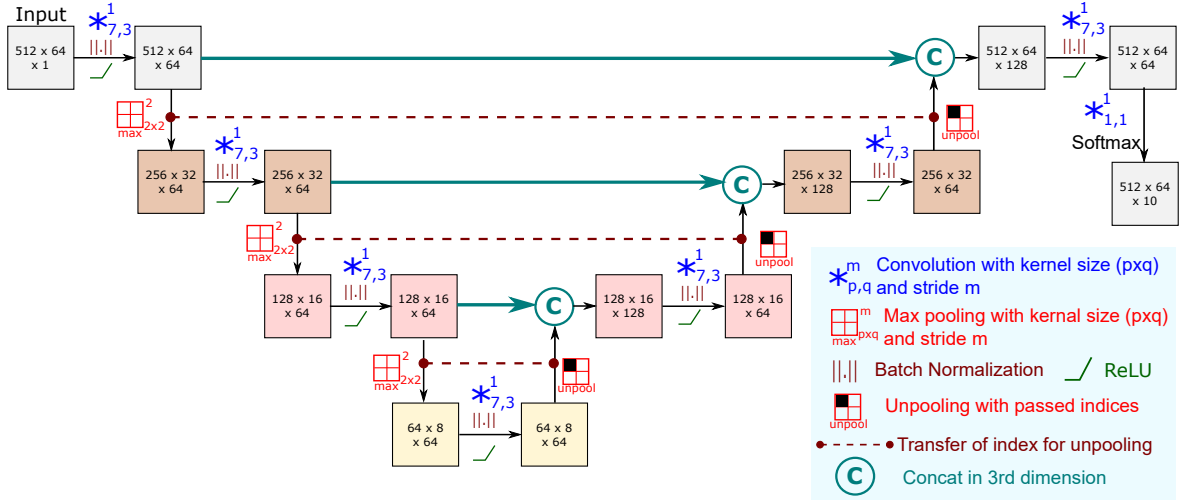


**Fig 3** Proposed fully convolutional ReLayNet architecture for retinal layer and fluid segmentation. The spatial resolution of the feature maps are indicated in the boxes. The symbols for the different operations are indicated to the right.

layer ensures that spatial information remains preserved in contrast to using bilinear interpolation for upsampling.<sup>20</sup> This is particularly important for the task of retinal layer segmentation as some retinal layers near the fovea region are just a few pixels thick and bilinear interpolation could potentially lead to highly diffused boundaries and hence unreliable estimation of layer thickness. This unpooling layer is followed by a skip connection that relays the output feature maps of the matched encoder block which is in turn concatenated with the unpooled feature maps within the concatenation layer. The advantage of such a skip connection is two folds: (i) it aids the transition from low to high dimensions by adding an information rich feature map from the encoder part, and (ii) it aids the flow of gradients to the encoder part, thus minimizing the risk of vanishing gradient training deep models. The concatenated feature map is followed by convolutional layer, batch normalization and ReLU. This densifies the sparse unpooled feature maps. The kernel size of convolution layer is kept constant at  $7 \times 3$  with appropriate padding similar to the encoder blocks.

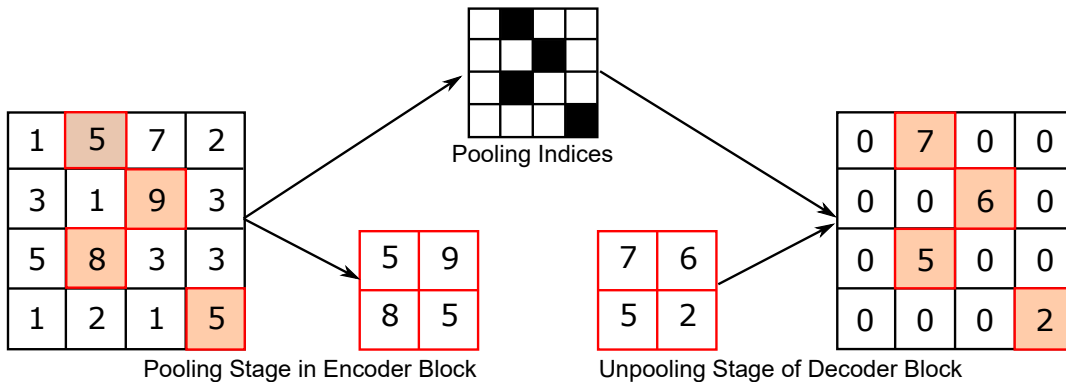


**Fig 4** Illustration of pooling and unpooling procedures. The pooling stage involves saving the intermediate pooling indices, which is leveraged in the unpooling stage preserving appropriate spatial locations. Unpooling involves mapping the values in the appropriate locations provided by the saved indices and rest is filled with zero.

### 3.3.3 Classification Block

The final decoder block is followed by a convolutional layer with  $1 \times 1$  kernels (used for reducing channels of the feature map without changing spatial dimensions) to map the 64 channel feature map to a 10 channel feature map (for 10 classes). At the end, a softmax layer estimates the probability of a pixel belonging to either of the 10 classes.

## 3.4 Training

### 3.4.1 Loss Functions

The ReLayNet is trained by optimizing the following two loss functions.

**Weighted multi-class logistic loss:** Cross-entropy provides a probabilistic similarity between the actual label and the predicted value at the current state of the network. The average cross-entropy of all the classes defines the logistic loss, which penalizes at each pixel location  $\mathbf{x}$  the deviation of the estimated probability  $p_l(\mathbf{x})$  from 1 and is defined as follows:

$$\mathcal{J}_{\text{logloss}} = - \sum_{\mathbf{x} \in \Omega} \omega(\mathbf{x}) g_l(\mathbf{x}) \log(p_l(\mathbf{x})) \quad (1)$$

where  $p_l(\mathbf{x})$  provides the estimated probability of pixel  $\mathbf{x}$  to belong to class  $l$ , and  $\omega(\mathbf{x})$  is the weight associated with pixel  $\mathbf{x}$ . where  $g_l(\mathbf{x})$  is a vector with one for the true label and zero entries for the others representing the ground truth probability of pixel at location  $\mathbf{x}$  to belong to class  $l$ . We utilize a weighted logistic loss for our application by assigning different weights to different pixels, in turn penalizing deviations at some important pixels (like boundary between two classes) much more than the others. This weighting scheme also aims at compensates for class imbalance. We discuss the weighting scheme in detail in Section 3.4.2.

**Dice loss:** Along with the multi-class logistic loss function which gives a probabilistic measure of how close the predictions are to the ground truth, we introduce Dice loss giving a count based estimate of the quality of segmentation. In a binary classification scenario, the Dice score is estimated as

$$Dice = \frac{2TP}{2TP + FP + FN} \quad (2)$$

Where  $TP$ ,  $FP$  and  $FN$  are the true positives, false positives and false negatives respectively. The non-differentiable nature of Eq. (2) restricts its usage in training deep neural networks as it cannot be optimized by gradient descent based methods. Alternatively, we use a differentiable approximation of dice loss, defined as follows:<sup>31</sup>

$$\mathcal{J}_{\text{dice}} = 1 - \frac{2 \sum_{\mathbf{x} \in \Omega} p_l(\mathbf{x}) g_l(\mathbf{x})}{\sum_{\mathbf{x} \in \Omega} p_l^2(\mathbf{x}) + \sum_{\mathbf{x} \in \Omega} g_l^2(\mathbf{x})} \quad (3)$$

### 3.4.2 Weighting scheme for Loss Function

Each pixel  $\mathbf{x} \in \Omega$  is associated with a weight  $\omega(\mathbf{x})$ , which expresses the relative importance of the pixel while computing the logistic loss. This weighting scheme is enforced to compensate for two important aspects. Firstly, pixels belonging to tissue transition zones (*i.e.* adjoining to the tissue boundaries) are the most challenging to be labelled as they are often diffused due to speckle noise. Therefore, regions should be deemed more important than homogeneous regions within the layers,



which is incorporated with the proposed weighting scheme. Secondly, gradients arising from small anatomical structures or under-represented classes with low prior probability ought to be boosted to compensate for the class imbalance within the training data, by selectively re-weighting their contributions.

For our problem, all the boundary regions between tissue types, estimated from the gradient of the label map, were boosted  $\omega_2$  times. To incorporate for the class imbalance, we boosted all the retinal layers and fluid, i.e. classes  $\mathbf{L} = \{2, \dots, 8, 10\}$ ,  $\omega_1$  times in comparison to the dominant background classes. Sample example has been illustrated in Fig. 5. The final weighting scheme to be used within Eq. (1) is defined as:

$$\omega(\mathbf{x}) = \omega_0 + \omega_1 \mathbf{I}(l(\mathbf{x}) = \mathbf{L}) + \omega_2 \mathbf{I}(|\nabla l(\mathbf{x})| > 0) \quad (4)$$

where  $\mathbf{I}(\text{logic})$  is a indicator function which is one if the (*logic*) is true, else returns zero. ' $\nabla$ ' represents the gradient operator.

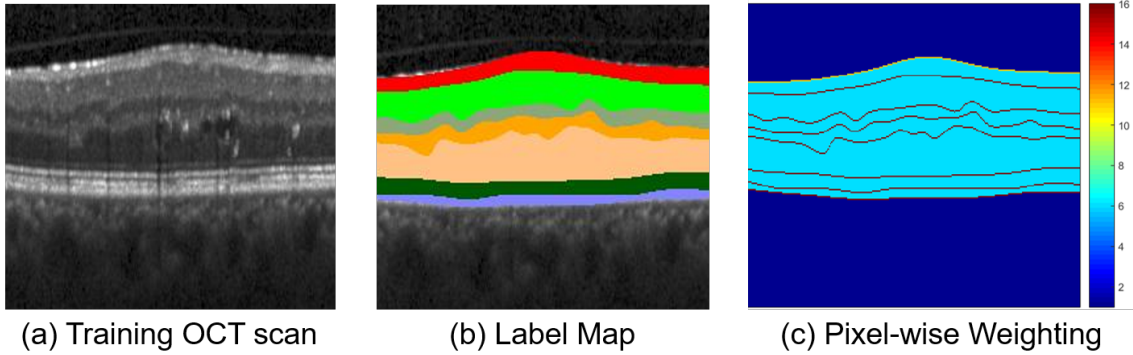


**Fig 5** Illustration of the weighting scheme for different pixels of a training B-scan OCT image. A sample OCT training B-scan is shown in (a), with its ground truth labels in (b) and the corresponding weights for training as heat map in (c)

### 3.5 Optimisation

During training the ReLayNet, we optimize the overall cost function given by a combination of logistic loss, dice loss and an additional weight decay term for regularization.

$$\mathcal{J}_{\text{overall}} = \lambda_1 \mathcal{J}_{\text{logloss}} + \lambda_2 \mathcal{J}_{\text{dice}} + \lambda_3 \|\mathbf{W}^{(\cdot)}\|_F^2 \quad (5)$$

with weight terms  $\lambda_1$ ,  $\lambda_2$  and  $\lambda_3$  and  $\|\mathbf{W}^{(\cdot)}\|_F$  represents the Frobenius norm on the weights  $\mathbf{W}$  of the ReLayNet. The training problem is to estimate the weights and bias  $\Theta = \{\mathbf{W}^{(\cdot)}, \mathbf{b}^{(\cdot)}\}$  associated with all the layers, so that to minimize the overall cost function:

$$\Theta^* = \underset{\Theta: \{\mathbf{W}^{(\cdot)}, \mathbf{b}^{(\cdot)}\}}{\text{argmin}} \mathcal{J}_{\text{overall}}(\Theta) \quad (6)$$

where  $\Theta^*$  is the optimal parameter set that minimizes the overall cost. This cost function is optimized using stochastic gradient descent and back propagation. The derivative of the cost function

w.r.t. the parameters  $\Theta$  is given by:

$$\frac{\delta \mathcal{J}_{\text{overall}}}{\delta \Theta} = \frac{\delta \mathcal{J}_{\text{overall}}}{\delta p_l(\mathbf{x})} \frac{\delta p_l(\mathbf{x})}{\delta \Theta} \quad (7)$$

The second term,  $\frac{\delta p_l(\mathbf{x})}{\delta \Theta}$  is estimated via chain rule by back propagating the gradients. The first term,  $\frac{\delta \mathcal{J}_{\text{overall}}}{\delta p_l(\mathbf{x})}$  is estimated as:

$$\frac{\delta \mathcal{J}_{\text{overall}}}{\delta p_l(\mathbf{x})} = \lambda_1 \frac{\delta \mathcal{J}_{\text{logloss}}}{\delta p_l(\mathbf{x})} + \lambda_2 \frac{\delta \mathcal{J}_{\text{dice}}}{\delta p_l(\mathbf{x})} \quad (8)$$

The derivative terms of the individual losses are derived as:

$$\frac{\delta \mathcal{J}_{\text{logloss}}}{\delta p_l(\mathbf{x})} = - \sum_{\mathbf{x} \in \Omega} \frac{\omega(\mathbf{x}) g_l(\mathbf{x})}{p_l(\mathbf{x})} \quad (9)$$

$$\frac{\delta \mathcal{J}_{\text{dice}}}{\delta p_l(\mathbf{x})} = -2 \frac{g_l(\mathbf{x}) (\sum_{\mathbf{x} \in \Omega} p_l^2(\mathbf{x}) + \sum_{\mathbf{x} \in \Omega} g_l^2(\mathbf{x})) - 2p_l(\mathbf{x}) (\sum_{\mathbf{x} \in \Omega} p_l(\mathbf{x}) g_l(\mathbf{x}))}{(\sum_{\mathbf{x} \in \Omega} p_l^2(\mathbf{x}) + \sum_{\mathbf{x} \in \Omega} g_l^2(\mathbf{x}))^2} \quad (10)$$

The learning parameters  $\Theta$  are updated by mini-batch stochastic gradient with momentum descent after every iteration as:

$$\Theta^t = \Theta^{t-1} - \eta^t \quad (11)$$

$$\eta^t = \rho \eta^{t-1} + \gamma \frac{\delta \mathcal{J}_{\text{overall}}}{\delta \Theta^{t-1}} \quad (12)$$

Here  $t$  denotes the current iteration,  $\rho$  is the momentum and  $\gamma$  is the learning rate for SGD. It should be noted that  $\rho$  and  $\gamma$  are very carefully chosen to obtain convergence.

## 4 Experimental Setup

### 4.1 Dataset

The proposed framework is evaluated on the Duke SD-OCT publicly available dataset for DME patients.<sup>17</sup> The dataset consists of 110 SD-OCT B-scan images of size  $512 \times 740$  obtained from 10 patients suffering from DME (11 B-scans per patient). The 11 B-scans per patient were collected centered at fovea and 5 frames on either side of the fovea (foveal slice and scans laterally acquired at  $\pm 2, \pm 5, \pm 10, \pm 15$  and  $\pm 20$  from the foveal slice). These 110 B-scans are annotated for the retinal layers and fluid regions by two expert clinicians. The details of the acquisition process is reported in.<sup>17</sup>

### 4.2 Experimental settings

Following the standard convention of splitting this dataset as reported in,<sup>17</sup> we divide the data with subject 1-5 in the training set and subject 6-10 in the testing set. This results in a total of 55 annotated B-scans for training and 55 B-scans for testing. We extensively augment the 55 training slices as detailed in Sec. 3.2 to train ReLayNet. The hyperparameters in loss function in Eq. (5) were set as  $\lambda_1 = 1$ ,  $\lambda_2 = 0.5$  and weight decay  $\lambda_3 = 0.0001$ . For our experiments we empirically set  $\omega_0 = 1$ ,  $\omega_1 = 5$  and  $\omega_2 = 10$ . The SGD optimization is performed in mini batches of size = 50.

During start of training the learning rate  $\gamma$  is set to 0.1 and is reduced by an order of magnitude after every 30 epochs. The training was performed with a momentum of  $\rho = 0.9$ . The training parameters are kept constant for all the deep learning comparative methods and baselines for fair comparison. All the networks were run till convergence. The training was conducted with expert 1 annotations and expert 2 annotation is used for validation purposes.

### 4.3 Comparative methods and baselines

The performance of the proposed ReLayNet is evaluated against state-of-the-art retinal OCT layer segmentation algorithms. Along with these traditional approaches we also compare with deep learning methods, U-Net architecture,<sup>21</sup> the state-of-the-art method for semantic segmentation on bio-medical images and FCN architecture,<sup>19</sup> one of the state-of-the-art method for semantic segmentation in computer vision community. The comparative methods are listed as follows:

1. CM-GDP: Graph based dynamic programming (GDP).<sup>15</sup>
2. CM-KR: Kernel regression with GDP (KR+GDP).<sup>17</sup>
3. CM-LSE: Layer specific structured edge learning with GDP (LSE+GDP).<sup>22</sup>
4. CM-Unet: U-Net architecture.<sup>21</sup>
5. CM-FCN: Fully Convolutional Network (FCN).<sup>19</sup>

The comparative methods CM-GDP, CM-KR and CM-LSE are graph based approaches while CM-Unet and CM-FCN are deep learning approaches. With the access to limited data available for training we reduced the depth of the designed architecture in comparison to the ones reported in the U-net paper.<sup>21</sup> Also, we kept the depth, kernel size, number of channels the same as our proposed architecture for fair comparison. It should be noted that the unique properties associated with the U-net architecture, i.e. the long skip connection and weighting scheme have also been preserved while comparing. The same is done for the FCN<sup>19</sup> architecture. The encoder part of our architecture is converted to a FCN tapping the feature maps at each pooling stages and bi-linearly upsampling them to estimate the segmentation.

Several plausible variations of the proposed ReLayNet framework have been set as baselines for comparison, to highlight the importance of each of the proposed contributions. All the baselines are detailed below, with the salient aspects of each baseline detailed in Tab. 1.

### 4.4 Evaluation metrics

The performance of the proposed framework in comparison to the defined comparative methods and baselines are evaluated based on 3 standard metrics reported on recent papers on retinal layer segmentation:<sup>17,22</sup>

1. **Dice Score:** This provides a similarity index of segmentation and the ground truth for each of the classes. This is a count based metric (True positives), dependent on the overlap between the segmented region and the ground truth.

**Table 1** Salient attributes of the proposed ReLayNet are depth of the architecture, loss function, skip connection and weighting scheme in loss function. Based on these attributes the following baselines are defined to investigate the importance for each of these attributes. The configuration of the baselines are indicated below.

	Architecture	Loss function	skip connection	Weighting scheme
BL-1	3 – 1 – 3	Dice + Logistic	×	✓
BL-2	3 – 1 – 3	Dice + Logistic	only LR skip	✓
BL-3	3 – 1 – 3	Dice + Logistic	only HR skip	✓
BL-4	3 – 1 – 3	Logistic	✓	✓
BL-5	3 – 1 – 3	Dice	✓	×
BL-6	2 – 1 – 2	Dice + Logistic	✓	✓
BL-7	4 – 1 – 4	Dice + Logistic	✓	✓
BL-8	3 – 1 – 3	Logistic	✓	×

2. **Estimated contour error for each layer:** This provides a similarity of the ground truth contour and the segmented contour evaluated by point wise similarity of the boundary co-ordinates depicting the contours. The mean absolute error in contour boundary is reported.
3. **Error in estimated thickness map for each layer:** Thickness of each of the retinal layers are important in making proper diagnosis regarding abnormality. We compared the mean absolute difference between the actual thickness maps to the segmented ones.

The lateral resolution of the OCT B-scans is between  $10.9\mu\text{m}$  to  $11.9\mu\text{m}$ .<sup>17</sup> As we are unaware of the exact lateral resolution corresponding to each B-scans, we report the contour and thickness error in pixels.

#### 4.5 Training and Testing time

The training and testing was performed in a Intel Core-i7 machine with a 12GB Tesla K40 Nvidia GPU. The code was implemented using the MATLAB based open source MatConvNet toolbox.<sup>32</sup> The network is trained for 50 epochs to converge which took approximately 4 hours. The testing time in GPU per B-scan is about 0.01 seconds, i.e. volume segmentation with around 500 B-scans can be achieved in around 5 seconds making it well suited for very fast for deployment and practical for real-time applications.

## 5 Experimental Observation and Discussion

### 5.1 Qualitative comparison of ReLayNet with comparative methods

Example segmentation of the proposed ReLayNet along with the defined comparative methods for an abnormal OCT B-scan with DME is presented in Fig. 6 and for a normal OCT B-scan in Fig. 7.

*Abnormal OCT B-scan:* This frame is one of the challenging examples due to two major aspects: (i) existence of accumulated fluid mass, (ii) the frame is near the fovea, thus the retinal layers are very thin (indicated by yellow arrow). Towards the right side of the frame, there exists a small pool of accumulated fluid indicated by a white box, which is very difficult to distinguish in the OCT frame. Our proposed ReLayNet successfully segments it, while CM-Unet, CM-FCN and CM-KR prediction fails to capture the small structure (shown with a white rectangular box in Fig. 6(b-d)). This might be due to the use of unpooling layers which are well suited for preserving the spatial information. Also, we can observe that near the fovea (indicated by yellow arrow), the predictions of CM-GDP is highly smoothened with lack of detail and particularly overpredicts

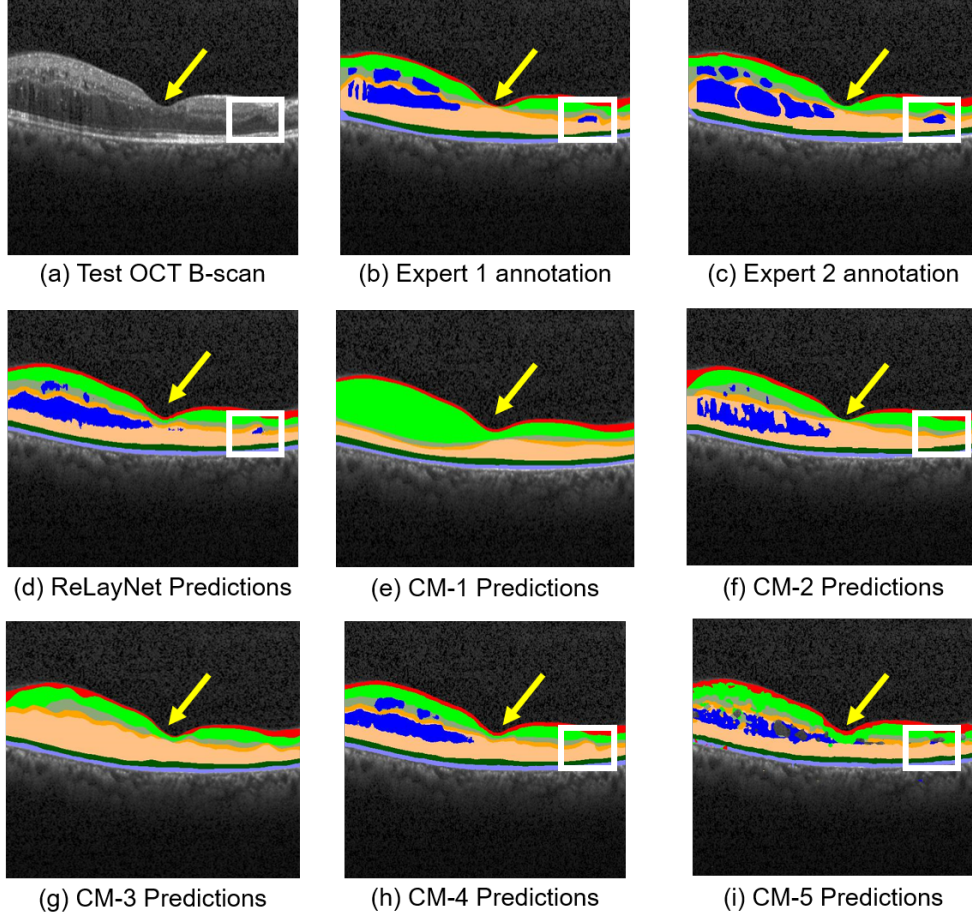
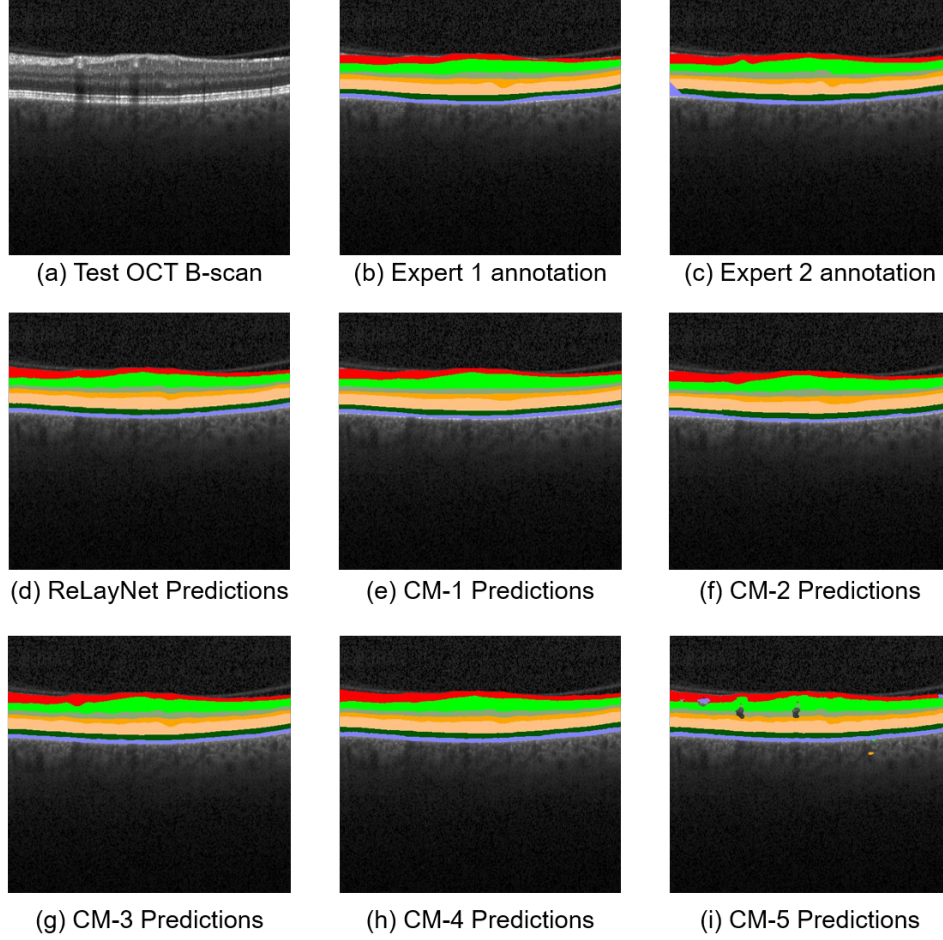


**Fig 6** Layer and fluid predictions of sample Test OCT B-scan near fovea with DME manifestation, shown in (a) with the expert 1 annotations in (b), expert 2 annotations in (c), ReLayNet predictions in (d) and predictions of the defined 5 comparative methods in (e-i). CM-GDP and CM-LSE doesn't include predictions for fluid. The fovea is indicated by the yellow arrow. The region with a small region of fluid mass is shown by a small white bounding box.

Class NFL-IPL and underpredicts the lower retinal layers. In comparison, CM-GDP and CM-LSE result in predictions with greater detail. However, these methods do not consider the presence of fluid while segmenting and the resultant thickness maps may be erroneous at locations proximal to fluid structures. We also observe that the segmentation of ReLayNet and CM-Unet are of high quality and comparable to that of another human expert, indicating the strength of F-CNN based deep learning frameworks for semantic segmentation in such applications. CM-FCN performs very poorly at the fluid class and suffers from high confusion between the Fluid and RbR class. This indicates towards the importance of encoder/ decoder based architectures and weighted loss





ONL-ISM: Outer Nuclear layer to Inner segment myeloid	OS-RPE: Outer segment to Retinal pigment epithelium
ISE: Inner segment ellipsoid	Accumulated Fluid
INL: Inner Nuclear Layer	ILM: Inner Limiting Membrane
OPL: Outer Plexiform Layer	NFL-IFL: Nerve Fiber Layer to Inner Plexiform Layer

**Fig 7** Layer and fluid predictions of sample Test normal OCT B-scan, shown in (a) with the expert 1 annotations in (b), expert 2 annotations in (c), ReLayNet predictions in (d) and predictions of the defined 5 comparative methods in (e-i).

function which FCN lacks in comparison to ReLayNet and CM-Unet.

*Normal OCT B-scan:* This frame exhibits a normal frame away from the fovea. We can observe a similar performance for all the comparative methods and low variation in performance. This observation indicates that the comparative methods have been trained fairly and the major distinction arises in the presence of pathology where such an objective segmentation tool is often needed.



## 5.2 Quantitative comparison of ReLayNet with comparative methods

### 5.2.1 Comparison with Graph-based Dynamic Programming Methods

Comparative methods CM-GDP, CM-KR and CM-LSE are the graph based dynamic programming methods proposed for retinal layer segmentation. We compare our proposed ReLayNet performance for the defined 3 metrics defined in Sec. 4.4. Comparing the segmentation efficacy with dice score as presented in Tab. 2, ReLayNet has the highest performance in 9 classes out of 10 with above 0.9 dice coefficient for RaR, ILM, NFL-IPK, ONL-ISM, ISE and OS-RPE layers. In the particular case of ONL-ISM layer, ReLayNet has the second best performance in dice (0.93) which is highly comparable to the best performing comparative method CM-LSE. Further, the OPL layer is the most challenging retinal layer to segment (evident from the low dice overlap of 0.74 between two expert observers). In this challenging layer, ReLayNet achieves an overall dice performance of 0.84 which is substantially improved over the other comparative methods with improvements of 0.17, 0.10 and 0.07 over CM-GDP, CM-KR and CM-LSE respectively. In addition to improved layer segmentation, we also observe substantial improvement in the segmentation of fluid masses and report a dice score of 0.77 which improves significantly from 0.63 dice observed for the closest comparative method CM-Unet. This reaffirms the superiority of ReLayNet to reliably segment both the retinal layers and underlying fluid masses.

Evaluation based on mean absolute difference in estimating layer thickness (metric 2), the proposed ReLayNet achieves the best performance for all the layers as reported in Tab. 3. CM-GDP has the worst performance in thickness estimation for layers ILM, NFL-IPL, OPL and ONL-ISM. CM-KR and CM-LSE exhibits similar performance and better than CM-GDP due to improvements incorporated in them. These methods however fail to match the performance of ReLayNet. ReLayNet has the highest absolute difference in thickness estimation for layer ILM (1.5 pixels). It outperforms CM-GDP, CM-KR and CM-LSE by margins of 2.50, 0.24 and 0.26 pixels respectively. This implies that ReLayNet is more robust for estimating layer specific thickness in comparison to graph based approaches especially for modality like OCT where a reliable estimate of thickness is challenging owing to the presence of speckle noise and imaging artifacts.

Based on estimation of the upper contour of each of the retinal layers, we also quantified the performance by mean absolute difference in contour estimation. ReLayNet exhibits the best performance for all the layers except ONL-ISM, where CM-LSE and CM-GDP outperforms the proposed method by a margin of 1.23 and 0.97 pixels. This is because CM-GDP and CM-LSE doesn't involve estimation of the fluid class. The presence of fluid masses, typically within ONL-ISM layer which challenges contour estimation for this layer. It can be observed that ReLayNet outperforms CM-KR by a margin of 0.39 pixels which also involves estimating fluid class.

### 5.2.2 Comparison with Deep Learning based Methods

We compare our proposed F-CNN against two of the most commonly used deep learning based semantic segmentation frameworks, U-net (CM-Unet) and FCN (CM-FCN) in Tab. 2, Tab. 3 and Tab. 4. Evaluating based on Dice scores, both CM-Unet and CM-FCN shows lower performance in comparison to the proposed ReLayNet. CM-Unet has the second best performance for 5 classes among all the comparative methods. ReLayNet significantly outperforms CM-Unet and CM-FCN in fluid segmentation by margins of 0.10 and 0.49 respectively in Dice score. CM-Unet exhibits the worst performance of 0.28 dice for fluid class in comparison to all the comparative methods.

**Table 2** Comparison with Comparative Methods and Expert 2 annotations by Dice Score. The best performance is shown by **bold**, the second best is shown by  $\star$  and the worst shown by  $\dagger$ . The numbers denoted as 'NA' are not provided in the respective manuscripts.

	RaR	ILM	NFL-IPL	INL	OPL	ONL-ISM	ISE	OS-RPE	RbR	Fluid
Proposed	<b>0.99</b>	<b>0.90</b>	<b>0.94</b>	<b>0.87</b>	<b>0.84</b>	0.93 $\star$	<b>0.92</b>	<b>0.90</b>	<b>0.99</b>	<b>0.77</b>
Expert 2	NA	0.86	0.90	0.79	0.74	<b>0.94</b>	0.86 $\dagger$	0.82 $\dagger$	NA	0.58
CM-GDP	NA	0.77 $\dagger$	0.77 $\dagger$	0.65 $\dagger$	0.67 $\dagger$	0.86 $\dagger$	0.87	0.82 $\dagger$	NA	NA
CM-KR	NA	0.85	0.89	0.75	0.74	0.93	0.87	0.82 $\dagger$	NA	0.53
CM-LSE	NA	0.87 $\star$	0.90	0.80	0.77	<b>0.94</b>	0.88	0.86 $\star$	NA	NA
CM-Unet	<b>0.99</b>	0.86	0.91 $\star$	0.83 $\star$	0.81 $\star$	0.91	0.90 $\star$	0.83	<b>0.99</b>	0.67 $\star$
CM-FCN	0.97 $\star$	0.81	0.84	0.72	0.71	0.88	0.89	0.86	0.98 $\star$	0.28 $\dagger$

Comparing the estimates of layer thickness, we observe a trend in performance concurrent with that reported for Dice scores. Although CM-Unet performs better than CM-FCN for most of the layers, we observe that for OS-RPE layer CM-Unet has the worst performance while CM-FCN has the second best performance. Comparing the performance for contour estimation, ReLayNet has lower error for all the layers, especially ONL-ISM layer where ReLayNet has its maximum error amongst all the retinal layers, it still outperforms CM-Unet and CM-FCN by margins of 0.04 and 0.75 pixels respectively.

Overall analysis shows that ReLayNet performs better than CM-Unet based on the introduction of key contributions including that of (i) Dice loss function and (ii) use Unpooling layer instead of Convolution transpose layer which differentiates ReLayNet from U-net architecture. Also, CM-FCN performs poorly in comparison to both CM-Unet and ReLayNet mainly due to absence of weighted loss function, which can be interpreted from low dice score of fluid class (probably due to class imbalance problem). Another distinguishing factor is the absence of the encoder and decoder architecture in CM-FCN, which provides a stage-wise transition from low resolution to high resolution for better semantic segmentation.

### 5.2.3 Comparison with Additional Human Expert Observer

We also compare the agreeability between the two human expert annotations (Expert 1 vs. Expert 2) and ReLayNet performance (ReLayNet vs. Expert 1) and report the observed metrics in in Tab. 2, Tab. 3 and Tab. 4. The low observer agreement between the two experts reflected particularly by the low dice scores in retinal layers INL (0.79), OPL (0.74), OS-RPE (0.82) and the fluid class (0.58) shows that the task of retinal segmentation is highly subjective and challenging. This substantiates our premise for the need for an objective solution. Comparing Expert 2 annotations to that learnt by ReLayNet, we can observe a higher agreement with the ground truth (Expert 1) for ReLayNet.

## 5.3 Importance of ReLayNet contributions

### 5.3.1 Importance of skip connections

In order to assess the importance of skip connections within the ReLayNet architecture, we defined a baseline (BL-1) with no skip connections and compared the segmentation performance against our proposed ReLayNet. The performances are reported from all the 3 defined metrics in Tab. 5, Tab. 6 and Tab. 7 respectively. Overall, we observe that ReLayNet outperforms BL-1 in segmentation performance of all the retinal layers and fluid masses. Particularly, a significant improvement

**Table 3** Comparison with Comparative Methods and Expert 2 annotations by Mean absolute difference in Layer Thickness (in pixels). The best performance is shown by **bold**, the second best is shown by  $\star$  and the worst shown by  $\dagger$ .

	ILM	NFL-IPL	INL	OPL	ONL-ISM	ISE	OS-RPE
Proposed	<b>1.501</b>	<b>1.201</b>	<b>1.001</b>	<b>1.317</b>	<b>1.352</b>	<b>0.625</b>	<b>0.921</b>
Expert 2	2.010	2.330	2.170	2.290	2.240	1.530 $\dagger$	1.540
CM-GDP	4.034 $\dagger$	4.045 $\dagger$	1.994	2.633 $\dagger$	5.507 $\dagger$	1.328	1.323
CM-KR	1.742 $\star$	2.321	2.277 $\dagger$	2.384	2.649	1.490	1.496
CM-LSE	1.764	2.250	2.195	2.315	2.314	1.268	1.231
CM-Unet	3.370	1.480 $\star$	1.270 $\star$	1.330 $\star$	2.105 $\star$	0.712 $\star$	1.814 $\dagger$
CM-FCN	2.070	2.445	2.146	1.912	2.814	1.302	1.222 $\star$

**Table 4** Comparison with Comparative Methods and Expert 2 annotations by Mean absolute difference in Layer contour boundary. The best performance is shown by **bold**, the second best is shown by  $\star$  and the worst shown by  $\dagger$ .

	ILM	NFL-IPL	INL	OPL	ONL-ISM	ISE	OS-RPE
Proposed	<b>0.85</b>	<b>1.14</b>	<b>1.22</b>	<b>1.35</b>	2.09	<b>0.81</b>	<b>0.81</b>
Expert 2	1.14	1.68	1.68	1.72	1.95	1.10 $\dagger$	1.27
CM-GDP	1.09	3.96 $\dagger$	5.94 $\dagger$	5.31 $\dagger$	1.12 $\star$	1.04	1.35 $\dagger$
CM-KR	1.32	1.70	2.01	2.16	2.48 $\dagger$	1.06	1.18
CM-LSE	0.97 $\star$	1.62	1.70	2.14	<b>0.86</b>	1.08	0.86 $\star$
CM-Unet	1.20	1.15 $\star$	1.26 $\star$	1.45 $\star$	2.13	0.86 $\star$	1.27
CM-FCN	1.73 $\dagger$	2.72	2.07	2.07	2.84	0.94	0.96

of 0.09 in dice score is observed in the fluid class. This is also reflected in the estimation of the retinal thickness and contour for the ONL-ISM layer where ReLayNet improves over BL-1 by a margin of 0.6 and 0.08 pixels respectively. This observed improvement is owed to the introduction of skip connections for feature map concatenation from encoder to decoder which provides a zero-resistance path for gradients to flow easily from deeper layers of decoder to shallower layers of encoder, thus aiding in proper weight updates through out the network as the training progresses.<sup>33</sup> Also, using the encoder feature maps within in the decoder stage provides additional contextual information aiding in better segmentation.

Further, we investigate the relative importance of different skip connections in the architecture. To evaluate this we defined two baselines of ReLayNet, one with only skip connections between the most low resolution feature maps of encoder and decoder (BL-2) and one with skip connections between the highest resolution (BL-3). The performance of ReLayNet as reported in Tab. 5, Tab. 6 and Tab. 7 is higher than both the variants BL-2 and BL-3 for all the metrics and for all the classes. An increase of 0.08 and 0.11 dice score for the fluid class is observed in comparison to BL-2 and BL-3 respectively. For ONL-ISM layer, a decrease in thickness estimation error of 1.6 and 1.5 pixel for BL-2 and BL-3 respectively is observed. Similarly a decrease of 0.15 and 0.12 pixels is observed in contour estimation. These observations affirm our premise that skip connections at all levels of resolution are highly contributory and introducing them induces significant improvements in network performance. Also, comparing the two baselines, we observe that in terms of dice, BL-3 tends to be marginally better than BL-2 but highly comparable in terms of the other metrics. However due to the complex nature of the gradient flows and the learning process, it is difficult to conclusively state that BL-3 is better than BL-2.

**Table 5** Comparison with Baselines by Dice Score. The best performance is shown by **bold**, the second best is shown by  $\star$  and the worst shown by  $\dagger$ . The baseline configuration is detailed in Table 1.

	RaR	ILM	NFL-IPL	INL	OPL	ONL-ISM	ISE	OS-RPE	RbR	Fluid
Proposed	<b>0.99</b>	<b>0.90</b>	<b>0.94</b>	<b>0.87</b>	<b>0.84</b>	<b>0.93</b>	<b>0.92</b>	<b>0.90</b>	<b>0.99</b>	<b>0.77</b>
BL-1	<b>0.99</b>	0.84 $\dagger$	0.92	0.83	0.80	0.89 $\dagger$	0.90	0.83 $\dagger$	<b>0.99</b>	0.68
BL-2	<b>0.99</b>	0.85	0.91	0.81 $\dagger$	0.78 $\dagger$	0.89 $\dagger$	0.89 $\dagger$	0.86	<b>0.99</b>	0.66 $\dagger$
BL-3	<b>0.99</b>	0.88	0.92	0.83	0.81	0.89 $\dagger$	0.90	0.87	<b>0.99</b>	0.69
BL-4	<b>0.99</b>	0.85	0.92	0.83	0.81	0.91	0.90	0.83 $\dagger$	<b>0.99</b>	0.72
BL-5	<b>0.99</b>	0.88	0.92	0.83	0.82 $\star$	0.92 $\star$	0.90	0.88	<b>0.99</b>	0.73
BL-6	0.97 $\star$	0.86	0.90 $\dagger$	0.81 $\dagger$	0.80	0.90	0.90	0.83 $\dagger$	<b>0.99</b>	0.68
BL-7	<b>0.99</b>	0.89 $\star$	0.93 $\star$	0.84 $\star$	0.82 $\star$	0.92 $\star$	0.91 $\star$	0.89 $\star$	<b>0.99</b>	0.76 $\star$
BL-8	<b>0.99</b>	0.86	0.90 $\dagger$	0.81 $\dagger$	0.78 $\dagger$	0.89 $\dagger$	0.89 $\dagger$	0.86	<b>0.99</b>	0.66 $\dagger$

**Table 6** Comparison with Baselines by Mean absolute difference (in pixel) in Layer Thickness. The best performance is shown by **bold**, the second best is shown by  $\star$  and the worst shown by  $\dagger$ . The baseline configuration is detailed in Table 1.

	ILM	NFL-IPL	INL	OPL	ONL-ISM	ISE	OS-RPE
Proposed	<b>1.501</b>	<b>1.201</b>	<b>1.001</b>	1.317	<b>1.352</b>	<b>0.625</b>	0.921
BL-1	2.903	1.332	1.290	1.441	1.951	0.732	1.881 $\dagger$
BL-2	1.860	1.400	1.350	1.340	2.920 $\dagger$	0.727	1.003
BL-3	1.730	1.700 $\dagger$	1.450	1.450	2.880	0.718	0.964
BL-4	3.050 $\dagger$	1.270 $\star$	1.250	1.320	1.800	0.658	1.619
BL-5	1.700	1.450	1.340	1.280 $\star$	3.180	0.660	0.860
BL-6	1.710	1.470	1.230 $\star$	<b>1.040</b>	2.270	0.690	<b>0.830</b>
BL-7	1.600 $\star$	1.580	1.320	1.420	1.520 $\star$	0.650 $\star$	0.960
BL-8	1.880	1.290	1.710 $\dagger$	1.710 $\dagger$	2.400	0.791 $\dagger$	0.840 $\star$

**Table 7** Comparison with Baselines by Mean absolute difference (in pixel) in Layer contour boundary. The best performance is shown by **bold**, the second best is shown by  $\star$  and the worst shown by  $\dagger$ . The baseline configuration is detailed in Table 1.

	ILM	NFL-IPL	INL	OPL	ONL-ISM	ISE	OS-RPE
Proposed	<b>0.85</b>	<b>1.14</b>	<b>1.22</b>	<b>1.35</b>	<b>2.09</b>	<b>0.81</b>	<b>0.81</b>
BL-1	1.59 $\dagger$	1.28	1.32	1.40	2.17	0.85	0.89
BL-2	1.13	1.26	1.34	1.42	2.24	0.83 $\star$	0.84
BL-3	1.12	1.25	1.33	1.45	2.21	0.84	0.85
BL-4	1.46	1.21	1.27	1.37 $\star$	<b>2.09</b>	0.83 $\star$	1.27 $\dagger$
BL-5	1.11	1.23	1.32	1.42	2.25	0.83 $\star$	0.82 $\star$
BL-6	1.32	1.56 $\dagger$	1.42	1.51	2.30	0.83 $\star$	0.84
BL-7	0.90 $\star$	1.17 $\star$	1.23 $\star$	1.37 $\star$	2.11 $\star$	<b>0.81</b>	0.82 $\star$
BL-8	1.25	1.47	1.46 $\dagger$	1.56 $\dagger$	2.37 $\dagger$	0.88 $\dagger$	0.89

### 5.3.2 Effect of joint loss functions

In the proposed ReLayNet, we leveraged a combination of two loss functions i.e. weighted logistic loss and dice loss simultaneous during training. To justify the joint loss function and to analyze the importance of each of the loss functions we defined two baselines, one with only the weighted logistic loss (BL-4) and one with only dice loss (BL-5). The performance of BL-4 and BL-5 are reported in Tab. 5, Tab. 6 and Tab. 7. We observe that the joint action of both the cost function provides better segmentation performance in comparison to each acting alone. A closer look at Tab. 5 for Dice scores reveals that thin retinal layers (particularly ILM and OS-RPE) can be better segmented with dice loss with scores of 0.88 and 0.88 respectively, in comparison to the weighted logistic loss (BL-4 vs. BL-5) with dice scores of 0.85 and 0.83 respectively. These two layers represent the two boundaries of retina and are very susceptible to be confused with the background classes. A similar observation is made for retinal thickness estimation (increase in error of 1.3 and 1.6 pixels for ILM and OS-RPE respectively) and contour estimation (increase in error of 0.3 and 0.5 pixels for ILM and OS-RPE respectively) comparing BL-4 vs. BL-5. Similarly for rest of the classes we observe similar performance for both BL-4 and BL-5 strongly indicative of the property of dice loss to learn in the presence for class imbalance. The effect is much more dominant with the joint action of dice loss along with logistic loss as proposed for ReLayNet.

### 5.3.3 Effect of depth of network

An important design factor to be considered while designing a deep neural network is the question of optimal depth. This is closely related to the underlying model complexity and ideally we need a network that is sufficiently deep to learn discriminative heirarchy of features to solve the segmentation problem at hand. However, we need to note that in scenarios of limited training data, a very deep network is more susceptible to overfit over a comparatively shallower counterpart. In light of this empirically accepted design rule, we explored three plausible architectures with varying depths as comparative baselines to the ReLayNet architecture. These architectures are addressed as  $x - 1 - x$ , which symbolizes an architecture with  $x$  encoder blocks, 1 low resolution convolutional block connecting the encoder and decoder followed by  $x$  matched decoder blocks. The architectures explored are  $2 - 1 - 2$  (BL-6),  $3 - 1 - 3$  (ReLayNet) and  $4 - 1 - 4$  (BL-7). The performance of all these architecture are reported in Tab. 5, Tab. 6 and Tab. 7. We observe that the dice performance of BL-6 deteriorates in comparison to ReLayNet. A decrease in 0.09 dice is observed for fluid class. A similar trend is observed for thickness estimation and contour estimation also. The overall increase in performance from BL-6 to ReLayNet is due to the deeper exploratory ability of more meaningful hierarchical features for segmentation.

Comparing ReLayNet vs. BL-7 with higher depth ( $4 - 1 - 4$ ), we can observe for most of the classes, the dice performance is almost same as ReLayNet except for the classes INL, OPL with an decrease of 0.03 and 0.02 dice scores. It exhibits the second best performance among all the baselines. A similar trend is observed in thickness and contour estimation. In thickness estimation, ReLayNet has the highest error for ILM class but it is lower than BL-7 by a margin of 0.1 pixel. Overall, ReLayNet provides better result than BL-7 by a small margin. This reduction in performance may be in part attributed to potential overfitting given limited annotated data and the associated higher model complexity of BL-7.

#### 5.3.4 Importance of pixel-wise weighted loss function

As illustrated in Sec. 3.4.2, we proposed to use a weighting scheme to compute the loss function, which selectively penalizes misclassification at the boundaries of retinal layers and compensates for class imbalance. To justify the use of such a weighting scheme, we set up baseline BL-8 with a model similar to the proposed ReLayNet but trained instead with normal logistic loss. We observe the performance as reported in Tab. 5, Tab. 6 and Tab. 7. Comparing against BL-4 (network with weighted logistic loss), we observe a fall of 0.06 dice score for the fluid class, which is the most under-represented class within the training data. In terms of thickness estimation, BL-8 exhibits the lowest performance for INL, OPL and ISE amongst all the baselines. For contour estimation, BL-8 reports the lowest performance for INL, OPL, ONL-ISM and ISE amongst all the baselines. This fall in performance reaffirms the importance of a weighting scheme within the loss function as motivated earlier in Section 3.4.2, for better segmentation at layer boundaries and compensating for class imbalance.

#### 5.4 Analysis of ETDRS grid across patients

Given a retinal OCT volume acquired for a specific subject, the thickness of the overall retina is generally reported as an Early Treatment of Diabetic Retinopathy Study (ETDRS) grid, providing the average thickness in 9 different spatial zones of the retina<sup>34</sup>. This grid represents a retinal OCT volume viewed from the top. It consists of 3 concentric circles of diameter 1 mm, 3 mm and 5 mm respectively centered at the fovea. The inner-most circle represents zone 1, centered at fovea indicating the most clinically significant region. The region near the fovea, between 1 mm and 3 mm circles is divided into zones 2, 3, 4 and 5. Also, the region between 3 mm and 5 mm circles is divided into zones 6, 7, 8 and 9 representing the regions of the eye far from fovea. The overall grid is illustrated in Fig. 8. The severity of an edema is assessed based on the thickness of the retina within each of these zones and also on which of the zones the thickness deviates from normal ranges.

We evaluate the thickness of the overall retina by combining Class 2 to Class 8. For all the 5 testing subjects (each containing 11 frames centered around the fovea), we computed the regions of each B-scans and under which zone it falls into from the ETDRS grid considering the lateral and azimuthal resolution of the OCT.<sup>17</sup> An example B-Scan is shown in Fig. 8(b) with its corresponding chord in the ETDRS grid (red line). The average absolute difference in overall retinal thickness of different comparative methods (CM-GDP to CM-FCN presented in Section 5.2) and ReLayNet from ground truth, for the 9 ETDRS zones are reported in Tab. 8. It must be noted that zones 9, 7 and zones 5, 3 interchanges their position depending on the eye is left or right. As, the information regarding the eye position was not provided, we show the result for only one case.

We observe that the performance of ReLayNet is significantly better than all the comparative methods for all the 9 zones. Zone 1 indicating the foveal region (most clinically significant) has a very low error of 0.3 pixels. CM-Unet has the second best performance for 4 out of 9 zones (zones 5, 7, 8, 9), especially in regions far from the fovea. The consistent performance of ReLayNet assures that it is reliable in estimating retinal thickness in all the spatial regions of the retina and is therefore deemed a good tool for estimating the ETDRS grid.



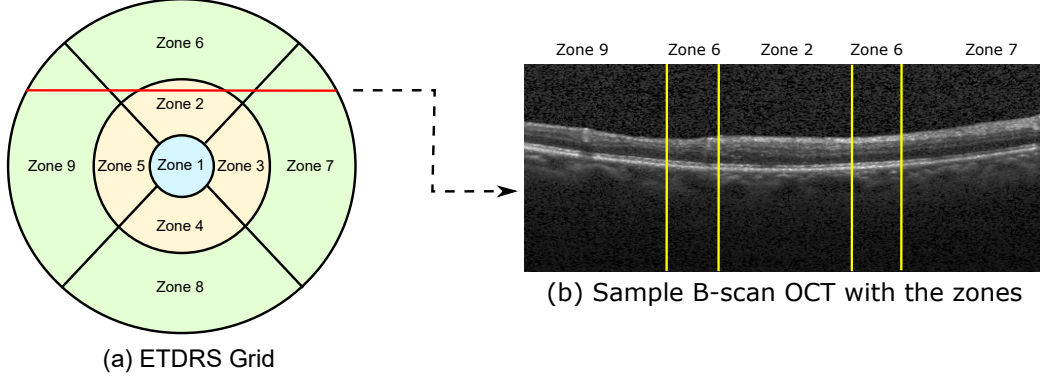


**Fig 8** Illustration of ETDRS grid with 9 zones as demarcated in (a). This represents the top view for a retinal OCT volume scan. A sample cross-sectional OCT B-scan slice corresponding to the red line in the ETDRS grid is shown in (b). The different regions of the B-scan corresponding to the different zones are indicating by yellow lines in (b).

**Table 8** Difference in retinal overall thickness (in pixels) for 9 zones in ETDRS grid across testing subjects. The best performance is shown by **bold**, the second best is shown by  $\star$  and the worst shown by  $\dagger$ .

	Zone 1	Zone 2	Zone 3	Zone 4	Zone 5	Zone 6	Zone 7	Zone 8	Zone 9
Proposed	<b>0.34</b>	<b>0.202</b>	<b>0.161</b>	<b>0.204</b>	<b>0.151</b>	<b>0.127</b>	<b>0.123</b>	<b>0.132</b>	<b>0.160</b>
CM-GDP	0.59	0.273	0.818 $\dagger$	0.375	0.698	0.889 $\dagger$	1.726 $\dagger$	0.849	2.565
CM-KR	1.77 $\dagger$	0.231	0.474	0.986 $\dagger$	1.252 $\dagger$	0.820	1.050	0.965 $\dagger$	2.576 $\dagger$
CM-LSE	0.64	0.230 $\star$	0.798	0.289 $\star$	0.803	0.775	1.189	0.471	2.036
CM-Unet	0.89	0.468 $\dagger$	0.434	0.500	0.368 $\star$	0.325	0.340 $\star$	0.327 $\star$	0.378 $\star$
CM-FCN	0.54 $\star$	0.405	0.398 $\star$	0.749	0.441	0.214 $\star$	0.443	0.797	0.461

## 6 Conclusion and Future Scopes

In this paper, we have proposed ReLayNet, an end-to-end fully convolutional neural network semantic segmentation of retinal OCT B-scan into 7 retinal layers and fluid masses. We train and validate the framework on a publicly available benchmark of expert annotated OCT B-scans acquired from 10 patients. The training of ReLayNet involves minimization of a combined loss comprising of weighted logistic loss and dice loss. To summarize, the key contributions presented in this paper are as follows:

1. To the best of our knowledge, ReLayNet is the first fully convolution approach to address OCT retinal layers and fluid segmentation.
2. Training of ReLayNet for semantic segmentation using dice loss along with weighted logistic loss is demonstrated to be highly effective for simultaneously segmenting thin retinal layers and the present fluid masses in case of diabetic macular edema.
3. Skip connections are a vital elements within the ReLayNet architecture as they provide rich contextual information and a path for easy flow of gradients across the network.
4. The usage of unpooling layers is a very important design choice for ReLayNet as it aids in preserving the spatial information which is particularly critical for fine-grained segmentation.

5. The complexity of the model (depth) for effective segmentation should be chosen based on the amount of available training data to leverage the strength of deep hierarchical features and avoiding over-fitting in the same time.
6. The segmentation test time is in the order of 0.01 seconds per OCT B-Scan, which allows for the method to find potential applications in interventional surgeries.

The proposed ReLayNet framework has been compared and validated against five state-of-the-art retinal layer segmentation methods including ones using graph-based dynamic programming<sup>15,17,22</sup> and deep learning.<sup>19,21</sup> Additionally, comparisons have been reported against eight incremental baselines validating each of the individual contributions. The evaluation was performed on the basis of three standard metrics including dice loss, retinal thickness estimation and deviation from layer contours. We demonstrate conclusively that ReLayNet exhibits superior performance in these comparisons and affirm that it can reliably segment even in the presence of a high degree of pathology which severely affects the normal layered structure of the retinal.

Towards the future work, we would extend ReLayNet into new scenarios like segmentation of OCT images acquired intraoperatively during retinal microsurgeries. Such a scenario is particularly challenging due to the poor resolution of the images and artifacts induced due to the presence of surgical tools. It must also be noted that the proposed model is vendor-specific i.e. deployable only to OCT scans acquired with the machines of the same manufacturer (Spectralis in our particular case) and tuned for a particular optical frequency. It has been observed that OCT scans across different vendors exhibit different optical properties, also termed as domain shift. The question of adapting ReLayNet to handle such a domain shift is open for further investigation.

## References

- 1 N. Nassif, B. Cense, B. H. Park, *et al.*, “In vivo human retinal imaging by ultrahigh-speed spectral domain optical coherence tomography,” *Optics letters* **29**(5), 480–482 (2004).
- 2 E. M. Anger, A. Unterhuber, B. Hermann, *et al.*, “Ultrahigh resolution optical coherence tomography of the monkey fovea. identification of retinal sublayers by correlation with semithin histology sections,” *Experimental eye research* **78**(6), 1117–1125 (2004).
- 3 D. Huang, E. A. Swanson, C. P. Lin, *et al.*, “Optical coherence tomography,” *Science (New York, NY)* **254**(5035), 1178 (1991).
- 4 A. T. Yeh, B. Kao, W. G. Jung, *et al.*, “Imaging wound healing using optical coherence tomography and multiphoton microscopy in an in vitro skin-equivalent tissue model,” *Journal of biomedical optics* **9**(2), 248–253 (2004).
- 5 B. Bouma, G. Tearney, H. Yabushita, *et al.*, “Evaluation of intracoronary stenting by intravascular optical coherence tomography,” *Heart* **89**(3), 317–320 (2003).
- 6 A. G. Roy, S. Conjeti, S. G. Carlier, *et al.*, “Lumen segmentation in intravascular optical coherence tomography using backscattering tracked and initialized random walks,” *IEEE journal of biomedical and health informatics* **20**(2), 606–614 (2016).
- 7 A. G. Roy, S. Conjeti, S. G. Carlier, *et al.*, “Bag of forests for modelling of tissue energy interaction in optical coherence tomography for atherosclerotic plaque susceptibility assessment,” in *Biomedical Imaging (ISBI), 2015 IEEE 12th International Symposium on*, 428–431, IEEE (2015).

- 8 A. G. Roy, S. Conjeti, S. G. Carlier, *et al.*, “Multiscale distribution preserving autoencoders for plaque detection in intravascular optical coherence tomography,” in *Biomedical Imaging (ISBI), 2016 IEEE 13th International Symposium on*, 1359–1362, IEEE (2016).
- 9 W. Weng, Y. Liang, E. S. Kimball, *et al.*, “Decreasing incidence of type 2 diabetes mellitus in the united states, 2007–2012: Epidemiologic findings from a large us claims database,” *Diabetes research and clinical practice* **117**, 111–118 (2016).
- 10 R. Klein and B. E. Klein, “Vision disorders in diabetes,” *Diabetes in America* **1**, 293 (1995).
- 11 V. Kumar, A. K. Abbas, N. Fausto, *et al.*, *Robbins and Cotran pathologic basis of disease*, Elsevier Health Sciences (2014).
- 12 M. F. Marmor, “Mechanisms of fluid accumulation in retinal edema,” *Documenta Ophthalmologica* **97**(3-4), 239–249 (1999).
- 13 J. A. Davidson, T. A. Ciulla, J. B. McGill, *et al.*, “How the diabetic eye loses vision,” *Endocrine* **32**(1), 107–116 (2007).
- 14 R. Kafieh, H. Rabbani, M. D. Abramoff, *et al.*, “Intra-retinal layer segmentation of 3d optical coherence tomography using coarse grained diffusion map,” *Medical image analysis* **17**(8), 907–928 (2013).
- 15 S. J. Chiu, X. T. Li, P. Nicholas, *et al.*, “Automatic segmentation of seven retinal layers in sdopt images congruent with expert manual segmentation,” *Optics express* **18**(18), 19413–19428 (2010).
- 16 P. P. Srinivasan, S. J. Heflin, J. A. Izatt, *et al.*, “Automatic segmentation of up to ten layer boundaries in sd-oct images of the mouse retina with and without missing layers due to pathology,” *Biomedical optics express* **5**(2), 348–365 (2014).
- 17 S. J. Chiu, M. J. Allingham, P. S. Mettu, *et al.*, “Kernel regression based segmentation of optical coherence tomography images with diabetic macular edema,” *Biomedical optics express* **6**(4), 1172–1194 (2015).
- 18 P. A. Dufour, L. Ceklic, H. Abdillahi, *et al.*, “Graph-based multi-surface segmentation of oct data using trained hard and soft constraints,” *IEEE transactions on medical imaging* **32**(3), 531–543 (2013).
- 19 J. Long, E. Shelhamer, and T. Darrell, “Fully convolutional networks for semantic segmentation,” in *Proceedings of the IEEE Conference on Computer Vision and Pattern Recognition*, 3431–3440 (2015).
- 20 H. Noh, S. Hong, and B. Han, “Learning deconvolution network for semantic segmentation,” in *Proceedings of the IEEE International Conference on Computer Vision*, 1520–1528 (2015).
- 21 O. Ronneberger, P. Fischer, and T. Brox, “U-net: Convolutional networks for biomedical image segmentation,” in *International Conference on Medical Image Computing and Computer-Assisted Intervention*, 234–241, Springer (2015).
- 22 S. Karri, D. Chakraborti, and J. Chatterjee, “Learning layer-specific edges for segmenting retinal layers with large deformations,” *Biomedical Optics Express* **7**(7), 2888–2901 (2016).
- 23 J. Tian, B. Varga, E. Tatrai, *et al.*, “Performance evaluation of automated segmentation software on optical coherence tomography volume data,” *Journal of biophotonics* **9**(5), 478–489 (2016).
- 24 H. Ishikawa, D. M. Stein, G. Wollstein, *et al.*, “Macular segmentation with optical coherence tomography,” *Investigative ophthalmology & visual science* **46**(6), 2012–2017 (2005).

- 25 M. Shahidi, Z. Wang, and R. Zelkha, “Quantitative thickness measurement of retinal layers imaged by optical coherence tomography,” *American journal of ophthalmology* **139**(6), 1056–1061 (2005).
- 26 D. C. Fernández, H. M. Salinas, and C. A. Puliafito, “Automated detection of retinal layer structures on optical coherence tomography images,” *Optics Express* **13**(25), 10200–10216 (2005).
- 27 F. Rathke, S. Schmidt, and C. Schnörr, “Probabilistic intra-retinal layer segmentation in 3-d oct images using global shape regularization,” *Medical image analysis* **18**(5), 781–794 (2014).
- 28 F. Rossant, I. Bloch, I. Ghorbel, *et al.*, “Parallel double snakes. application to the segmentation of retinal layers in 2d-oct for pathological subjects,” *Pattern Recognition* **48**(12), 3857–3870 (2015).
- 29 L.-C. Chen, G. Papandreou, I. Kokkinos, *et al.*, “Deeplab: Semantic image segmentation with deep convolutional nets, atrous convolution, and fully connected crfs,” *arXiv preprint arXiv:1606.00915* (2016).
- 30 S. Ioffe and C. Szegedy, “Batch normalization: Accelerating deep network training by reducing internal covariate shift,” *arXiv preprint arXiv:1502.03167* (2015).
- 31 F. Milletari, N. Navab, and S.-A. Ahmadi, “V-net: Fully convolutional neural networks for volumetric medical image segmentation,” *arXiv preprint arXiv:1606.04797* (2016).
- 32 A. Vedaldi and K. Lenc, “Matconvnet: Convolutional neural networks for matlab,” in *Proceedings of the 23rd ACM international conference on Multimedia*, 689–692, ACM (2015).
- 33 M. Drozdal, E. Vorontsov, G. Chartrand, *et al.*, “The importance of skip connections in biomedical image segmentation,” in *International Workshop on Large-Scale Annotation of Biomedical Data and Expert Label Synthesis*, 179–187, Springer (2016).
- 34 G. Panozzo, B. Parolini, E. Gusson, *et al.*, “Diabetic macular edema: an oct-based classification,” in *Seminars in ophthalmology*, **19**(1-2), 13–20, Taylor & Francis (2004).